Volcanic activities triggered or inhibited by resonance of volcanic edifices to large earthquakes

Atsuko Namiki[1,2*], Eleonora Rivalta[2], Heiko Woith[2], Timothy Willey[2-4], Stefano Parolai[5], and Thomas R. Walter[2]

[1] *Graduate School of Integrated Arts and Sciences, Hiroshima University, Higashi Hiroshima, 739-8521 Japan*

[2] *GFZ German Research Centre for Geosciences, 14473 Potsdam, Germany*

[3] *Geosciences, University of Montana, Missoula, Montana 59812, USA*

[4] *Earth and Environmental Science, University of Potsdam, 14469 Potsdam, Germany*

[5] *Istituto Nazionale di Oceanografia e di Geofisica Sperimentale, Borgo Grotta Gigante, 42/c, 34010 Sgonico TS, Italy*

**correspondence to: namiki@hiroshima-u.ac.jp*

This PDF file includes:

Extended Text Section 1 to 6
Supplementary Figs.DR1 to DR15
Table DR1 to DR2
Captions for Movies DR1 to DR5
Reference list

Other Supplementary Materials for this manuscript includes the following:

Movies DR1 to DR5

Figs.DR1-DR4 provide the supplementary information of experimental methods, physical properties of our gel. Figs.DR5-DR12 are the additional results and analysis of experiments, Figs.DR13-DR15 are materials to apply our experimental results to natural volcanic edifices. Table DR1 is a list of experimental conditions. Table DR2 compares our experiments and natural volcanoes. Movies DR1-DR4 and DR5 provide the moving images of experiments and calculation, respectively.

Extended text

1. Extended Experimental Methods

We simulate crack propagation by injecting fluid into an elastic agar gel, which is chosen as a rock analogue (Fig.DR1). Agar is a transparent gel, similar to gelatin, used in many experimental simulation studies of dike propagation in the crust (e.g., Takada, 1990; Sumita and Ota, 2011; Kavanagh et al., 2013). The agar solution is solidified in a container with a 0.14 m x 0.14 m cross-sectional area, and is covered with a mold, shaped as a two-dimensional ridge with a variable height, with slopes of 72º (Fig.DR2). By removing the mold, we obtain an agar gel with a mountain-shaped free surface.

We use 0.4-0.8 wt.% agar solutions (Ina Food Industry, UM-11S), and add 33 wt.% table sugar on the total to increase the shear modulus and transparency of the agar gel. This results in a shear modulus of 200-1300 Pa, yield stress of 500-7000 Pa, and a density of ρ =1134-1144 kg m^{-3} (Fig.DR3, Table DR1). The rheology is measured by imposing oscillatory deformation, allowing us to calculate the solid-like component $G'$and the liquid-like component G''. We use G' as the shear modulus G. The ratio of $Q^{-1} = G''/G'$ is attenuation and approximately $Q^{-1}\sim10^{-1}$for our gel. We also estimate $Q^{-1}$by measuring the acceleration at the top of the gel edifice (Fig.DR4). When the imposed oscillation stops, the amplitude of the measured acceleration decreases with time. By fitting this attenuation curve, we obtain $Q^{-1}\sim 0.16$ which is similar to that obtained by the rheology measurement. Our gel has a higher Q^{-1} than typical country rock $Q^{-1}\sim10^{-3}$ (e.g., Liu et al., 2014). The yield stress 500-7000 Pa is measured by rotating a vane spindle in the agar gel, as shown in Fig.DR3, a technique used in Sumita and Ota (2011). Fig.DR3C suggests that this agar gel yields at a strain of approximately 1.

We inject buoyant fluids from the bottom by using needles with a length of 25-70 mm and an inner diameter of 0.5-1.7 mm. As a buoyant fluid, we use air with a density of $\rho_\mathrm{i} = 1$ kg m^{-3} and a viscosity of 2×10^{-5} Pa s, water or sugar solution (0-25 wt.%) with a density of ρ_i =1000-1120 kg m^{-3} and a viscosity of ~10^{-3} Pa s, or a mixture of sugar solution and air bubbles. When we use a mixture of air bubbles and water, we add 3.7 wt.% of cellulose to increase the liquid viscosity of the fluid (0.9 Pa s) to prevent segregation of the bubbles from the liquid. However, some bubbles separate from the liquid during injection. We calculate the volume fraction of bubbles

(4-5 vol.%) using the areal fraction of bubbles in the photograph of the crack, assuming a uniform thickness. The buoyant liquid is dyed red with food coloring.

The orientation of the crack is controlled by the truncation of the needle tip (e.g., Takada, 1990). The growth of the crack is observed from three directions, the front, side, and top by using cameras recording at 30-240 frames per second and with a resolution of 512x384 or 1920x1080. The front camera is mounted on the shaking table and others are fixed to the ground. We qualitatively monitor the stress perturbations through photoelasticity by locating polarizer sheets in front and behind the gel edifice and using white backlight.

We impose horizontal oscillations on the gel edifice, with a shaking table (GeoSIG GSK-166, GFZ Potsdam Bubble lab), with a displacement of approximately $A\sin(\omega t)$, where A is the amplitude, $\omega = 2\pi f$ is the angular frequency, f is the imposed frequency, and t is time. We calibrated the imposed displacement through visual observations. The acceleration, measured by a sensor on the shaking table, shows sinusoidal signals with noisy high frequency modes. We test displacement amplitudes A of 1, 3, and 10 mm. For each displacement value, we increase frequency f step-by-step in the sequence denoted in Table DR1. Our experiments are conducted close to the upper limit of the loading for the shaking table, $A\omega^2 < g$, where $g = 9.8$ m s^{-2} is gravitational acceleration. As a result, we cannot explore cases where both the amplitude and frequency of shaking are simultaneously large.

We measure the pressure fluctuation of the gel 10 mm above the bottom of the container (Fig.DR1) by using a pressure transmitter (Keller PR-33X). We manually synchronize the visual images and sensor measurements at the beginning of the experiment.

The procedure of the experiment is as follows. We solidify the gel in a refrigerator for one night and leave it at room temperature for at least 4 hours. After the gel has adjusted to the room temperature, we fix the tank onto the shaking table and remove the mold. We then inject the buoyant fluid from the bottom. The fluid either ascends or stalls in the gel; the gel edifice is shaken in both cases. Depending on the experiment, the ascent resumes, the ascent velocity increases, or the direction of the fluid migration changes upon shaking. We evaluate those cases as “triggered”; i.e., the shaking is effective in assisting the crack propagation. If the buoyant fluid has

not yet reached the summit or walls of the gel after the shaking, we sometimes inject additional buoyant fluids, and then shake it again. We repeat this until the gel breaks.

2. Flow rate of fluid within the preexisting crack

Ascent of a fluid-filled crack involves fracturing at the tip and simultaneous fluid flow into the crack tip. The fluid flow widens the crack tip to cause a further fracturing. If the required stress for a fracturing is low enough, the viscous resistance of the fluid flow regulates crack ascent (e.g., Lister and Kerr, 1991). In gelatin experiments, especially those involving air as the injected fluid, crack ascent is regulated by fracturing (Kavanagh et al., 2013). The question whether magma propagation in nature is regulated by the viscosity of magma or the fracture toughness of rock has been long debated in literature (Rubin, 1995). The issue, which revolves around estimates of rock fracture toughness carried out in-situ vs. in the laboratory, has been thoroughly discussed in the light of recent progress and formalized in non-dimensional expressions comparing energy expenditure by viscous flow to fracturing (Rivalta et al., 2015). Using typical parameters from nature, it emerges that for natural dikes these are end-member behaviors: the propagation of comparatively short fractures fed at high rate with high-viscosity magma (e.g. andesite or rhyolite) are regulated by the fluid viscosity, while long (km-sized) fractures fed at low rate with low-viscosity magma (basalt), or lower viscosity fluids, are regulated by fracturing (Rivalta et al., 2015). Thus, we expect our experiments to be well-scaled to simulate the propagation of cracks filled with hydrothermal fluids or basaltic magma, while the approximation may be less effective in simulating viscous-dominated crack propagation.

In order to further support this argumentation, we here estimate the fluid flow velocity inside the crack to show that fluid flow is fast enough not to regulate crack ascent. The ascent velocity of a fluid with a viscosity of μ in a crack with a width of δ and a pressure gradient of $\Delta\rho g$, where $\Delta\rho = \rho - \rho_{\mathrm{i}}$ is the density difference between the outside and inside the crack, is written as (e.g., Lister and Kerr, 1991; Turcotte and Schubert, 2014)

$$u = \frac{\Delta\rho g \delta^2}{12\mu}.$$

Air as an internal fluid, with $\mu = 2 \times 10^{-5}$ Pa s and $\Delta\rho = 10^3$ kg m^{-3}, can ascend inside a crack with $\delta = 10^{-3}$ m, at a velocity of 40 m s^{-1}. In contrast, water as an internal fluid with $\mu = 10^{-3}$ Pa s and $\Delta\rho = 10^2$ kg m^{-3}, can ascend inside a crack with a same thickness of $\delta = 10^{-3}$ m, at a velocity of 0.08 m s^{-1}. Here, $\delta = 10^{-3}$ m is the typical thickness of the crack shown in Fig.1 estimated from its volume and area. Thus, the estimated ascent velocity of the fluids in the previously existing fracture with a sufficient thickness is much faster than that observed in Fig.1. In addition, the difference of the viscosity and density of internal fluid varies ascent velocity as much as 500 times.

We thus conclude that the ascent velocity of the fluid-filled crack at the edifice base is regulated by fracturing rather than fluid flow. Similarly, this must be the case in the natural volcanic edifice, where the volcanic edifice modifies the vicinal stress field. We note that the difference of the estimated flow velocity between air and water may be able to affect the eruptive location. The less viscous air flows into the narrow crack tip faster than water, so the air-filled crack can erupt from the top of the edifice.

3. Estimation of the stress field

Crack propagation depends on the surrounding stress field, including that generated by the surface topography and the magma chamber as a pressurizing source (e.g., Pinel and Jaupart, 2000; Muller et al., 2001,Watanabe et al., 2002; Karlstrom et al., 2009; Maccaferri et al., 2011; Roman et al., 2014; Rivalta et al., 2015; Pinel et al., 2017). The inertia force induced by the shaking ($MA\omega^2$) acting on the gel edifice causes stress in the edifice, where $M = \rho(W + W_t)WH/2$ is the mass of the gel edifice, $W$is the width at the base, W_t is the width of the top, and $H$is the height of the gel edifice (Namiki et al., 2016). The stress generated in the gel edifice is defined by the areal inertia force. If horizontal shear deformation acts on the base of the edifice, the inertia force per unit area becomes

$$\sigma_b = \frac{MA\omega^2}{W^2} = \frac{\rho\left(1 + \frac{W_t}{W}\right)HA\omega^2}{2}, \quad (\text{eq. DR1})$$

where W^2 is the area of the edifice's base. In this formulation, we neglect the bending of the edifice. In natural conditions, the bending of the volcanic edifice is negligible, unlike in our experiments, so this assumption is relevant for natural conditions.

In Fig. DR8 and Fig. DR9, we calculate the time evolution of the stress field in the gel edifice. The maximum stress is approximately 300 Pa at the center of the gel,

without a crack. This value is achieved when the initially generated compressional waves collide at the middle of the gel edifice. After that, the amplitude of the oscillating stress reduces. On the other hand, the stress (σ_b) in this experiment estimated by Eq.(DR1) is 150 Pa. When there exists a crack in the middle of the gel edifice, the maximum stress at the crack tip is close to 3000 Pa (Fig.DR9), while that at the crack surface becomes less than 100 Pa (Fig.DR8), suggesting focusing of stress. Willey (2017) uses the images of Fig.2, and estimates the stress field in the gel edifice by using photoelasticity. The calculated absolute stress is of similar orders of magnitude to σ_b in Eq.(DR1), but is slightly larger. This discrepancy may have arisen by repeated acceleration through the oscillation, which amplifies the elastic wave. In Fig. DR8, the stress is generated only by the initially imposed velocity. We thus consider Eq.(DR1) to be a good minimum estimate of the stress generated in the oscillating edifice.

The average stress, σ_b, generated by a volcanic edifice, with $H = 2$ km and a density of 2000 kg m^{-3}, resonating with an oscillation with an amplitude of $A = 0.5$ m (Koketsu et al., 2011) and a frequency of 0.1 Hz, is ~0.4 MPa. This value is similar or larger than the stress changes estimated to trigger volcanic unrest (Manga and Brodsky, 2006; Fujita et al., 2013), and is of the same order of magnitude estimated for the stress change caused by surface waves in Yukutake et al., (2013).

4. Evaluation of resonance frequencies

We estimate the resonance frequency of our gel and volcanic edifice using three methods.

1) Ratio of the shear wave velocity v_s and the width of the edifice base W,

$$f \sim 0.7 \frac{v_s}{W} \ . \qquad \text{(eq. DR2)}$$

The amplification of oscillation, induced by an earthquake at the top of a hill, has been observed when the oscillation frequency is in the range of $0.6 - 0.8$ times v_s/W (Geli et al., 1988). An analytical method shows that the prefactor is approximately constant, 0.7, when the edifice has the height/width ratio, $H/W < 0.5$ (Paolucci, 2002).We consider this estimate is appropriate to natural volcanic ranges.

2) In some of our experiments, the gel edifice has a trapezoidal shape exceeding $H/W > 0.5$. Towhata (2008) takes account of this shape and solves the

equation of motion for horizontal shaking by assuming a harmonic oscillation. The amplification produced by the topography is derived as

$$S(\omega) = \frac{\frac{2v_s}{\pi\omega z_0}}{\sqrt{\left[J_0\left(\frac{\omega(z_0+H)}{v_s}\right)Y_1\left(\frac{\omega z_0}{v_s}\right) - J_1\left(\frac{\omega z_0}{v_s}\right)Y_0\left(\frac{\omega(z_0+H)}{v_s}\right)\right]^2 + \left[J_1\left(\frac{\omega(z_0+H)}{v_s}\right)Y_1\left(\frac{\omega z_0}{v_s}\right) - J_1\left(\frac{\omega z_0}{v_s}\right)Y_1\left(\frac{\omega(z_0+H)}{v_s}\right)\right]^2}}, \quad \text{(eq.DR3)}$$

where J and Y are the Bessel functions of the first and second kinds, and z_0 is the height between the top of the trapezoidal edifice and the hypothetical vertex of a triangular edifice shape (Fig.DR1). We calculate the amplifications following this equation and plot them in Fig.DR12. The frequencies where amplifications become local maxima are resonance frequencies, and the lowest frequency among them is the fundamental mode.

3) We numerically calculate the eigen frequencies of the 2D trapezoidal shape by solving the wave equation under harmonic oscillation using COMSOL Multiphysics (Fig.DR8). This method reveals various deformation patterns some of which are similar to those observed in the experiments whereas others are not. We thus selected the deformation patterns similar to those observed in experiments (Fig.DR8), and listed them in Table DR1.

Numerically calculated resonance frequencies are close to those estimated by Eq.(DR2) and Eq.(DR3), validating the reliability of these equations. We use Eq.(DR2) for natural volcanic ranges and Eq. (DR3) for our gel edifice, because of low and high aspect ratios (H/W), respectively.

5. Flow velocity inside the crack

The flow of a fluid with velocity u in a crack, with a length of L and a thickness of δ, under a time dependent stress σ_b, oscillating with a frequency of f, should not be in a steady state. The force $\rho_i uf$ acting on the fluid with a density of ρ_i under the acceleration uf will be balanced by the summation of the stress gradient $\frac{\sigma_b}{L}$, viscous resistance $-\frac{\mu u}{\delta^2}$, and buoyancy force $\Delta\rho g$ resulting in

$$u \propto \frac{\frac{\sigma_b}{L} + \Delta\rho g}{\rho_i f + \frac{\mu}{\delta^2}}. \quad \text{(eq. DR4)}$$

In Eq.(DR4), frequency f appears in the denominator, indicating that high frequency oscillations prevent fluid flow. When $\rho_{\mathrm{i}} f \gg \frac{\mu}{\delta^2}$, the fluid flow is regulated by the high frequency. For our experiment in Fig.3, $\rho_{\mathrm{i}} = 10^3$ kg m^{-3}, $\mu = 10^{-3}$ Pa s, $\delta \sim 10^{-3}$ m, suggesting that the frequency preventing the fluid flow is $f \gg 1$Hz. This estimate is consistent with our observations; fluid migration is not remarkable during high frequency oscillations $f > 10$ Hz.

In natural conditions, assuming a magma density of $\rho_{\mathrm{i}} = 3 \times 10^3$ kg m^{-3}, a magma viscosity of $\mu = 10^3$ Pa s, and a dyke/sill thickness of $\delta \sim 1$ m, a $f \gg 0.3$Hz prevents the fluid flow. We note that the velocity estimated by Eq.(DR4) is much faster than that in our experiments. The crack is thinner at the tip thereby obstructing the fluid flow, Eq.(DR4) does not take this into account, leading to this discrepancy.

6. Resonance of a natural volcanic range

In our experiments, the gel edifice has a higher aspect ratio (H/W) compared to that of natural volcanic edifices. In addition, the gel edifice is surrounded by an acrylic tank, which may amplify the elastic wave caused by the resonance. In order to quantify potential resonance effects in nature, we simulate a more realistic condition numerically in Fig.DR14, in which the volcanic range has similar dimensions of those in Tohoku, and there is no scattering source. Actual seismic waves cause shaking not only in the horizontal directions but also in the vertical direction. Indeed, Rayleigh waves usually generate large displacement in the vertical direction. Therefore, we also simulate shaking in the vertical direction.

In Fig.DR14, the amplification of the displacement and the stress focusing by the existence of surface topography occurs in both the horizontal and vertical oscillations. We note that the vertical oscillation generates compression and extension in the vertical direction. This is the same for our experiment, but rotated 90°. If a sill (horizontal magma lens) or hydrothermal system exists beneath the volcanic range, such vertical oscillation would squeeze out the magma or hydrothermal fluid laterally, likely resulting in subsidence. Horizontal magma lenses such as sills are frequently present beneath volcanic edifices because of stress focusing (e.g., Watanabe et al., 2002; Roman et al., 2014; Rivalta et al., 2015; Pinel et al., 2017).

Natural seismic waves are not monochromatic and contain various wavelengths. In Fig.DR14, the horizontal shaking causes stress deviation with various wavelength. If oblique faults exist beneath the volcanic edifice, they can amplify the

stress (e.g., Brune, 1996; Gabuchian et al., 2017). We thus consider that similar phenomena to our experiments can occur beneath a natural volcanic range.

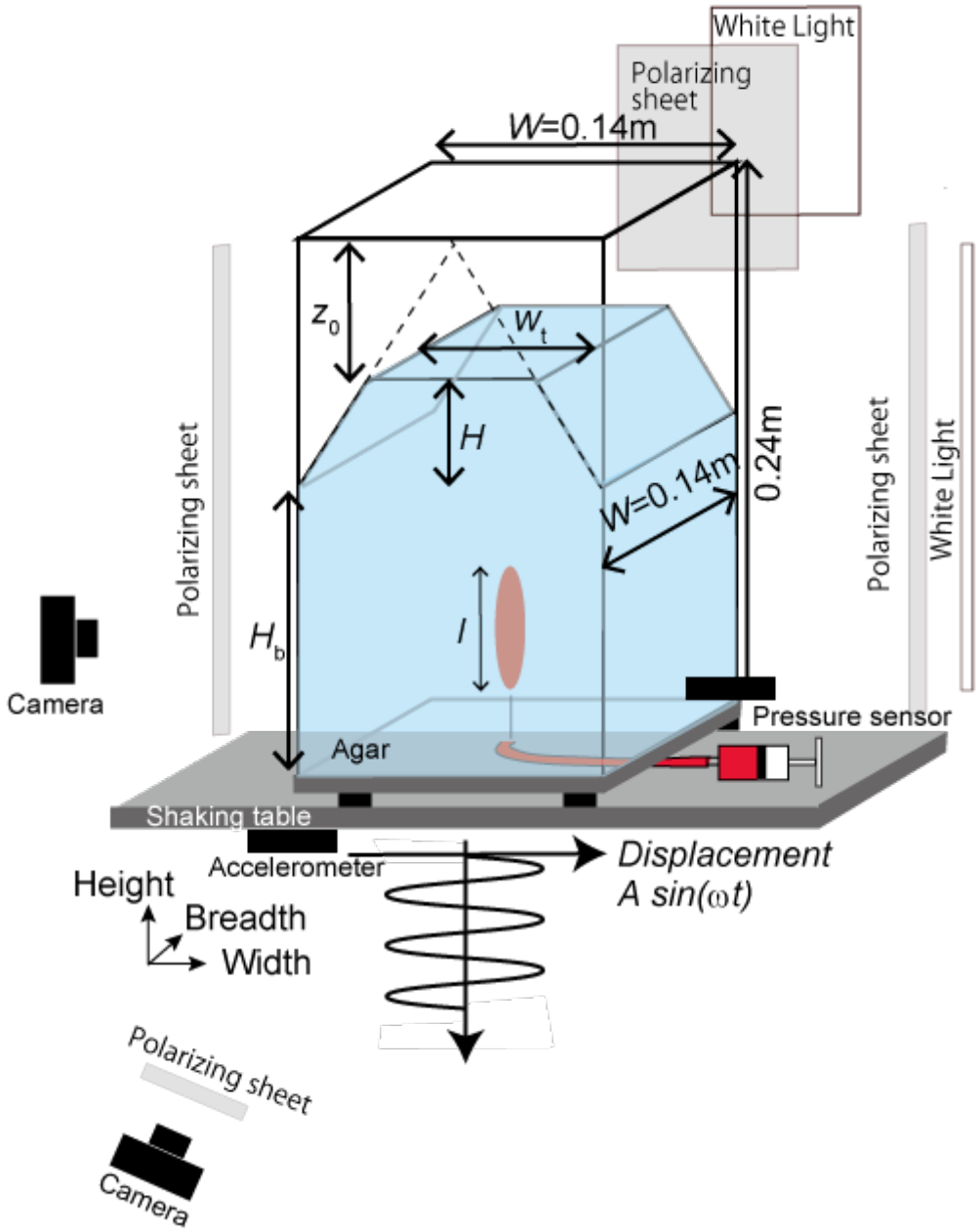

Figure DR1.

Schematic diagram of the experimental apparatus. A mountain-shaped, solidified agar gel in an acrylic tank, with a width and breadth of 0.14 m above a shaking table, is horizontally shaken with displacement of $A\sin(\omega t)$, where A is the displacement amplitude of the oscillation, t is time, $\omega = 2\pi f$, and f is frequency.

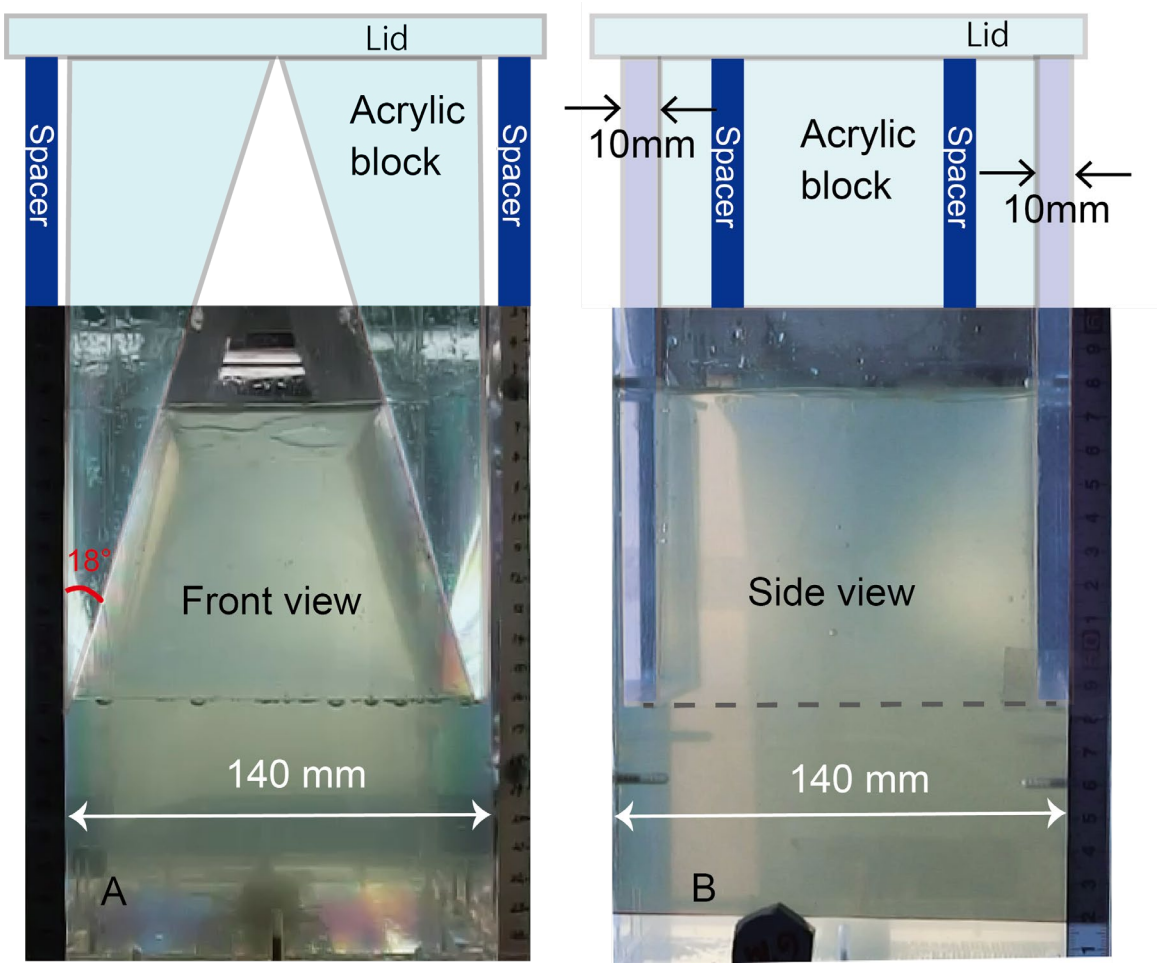

Figure DR2.

Pictures and illustrations of the solidified agar gel in (A) front and (B) side views. By locating the acrylic block in the agar solution during the solidification, we obtain the two dimensional trapezoidal agar gel. The gel edifice is separated from the tank wall by 10 mm by inserting an acrylic plate (side view). The height of the gel edifice can vary by changing the size of the spacers affixed to the lid. The gel edifice, obtained after removing the lid, is shown in Fig.DR10.

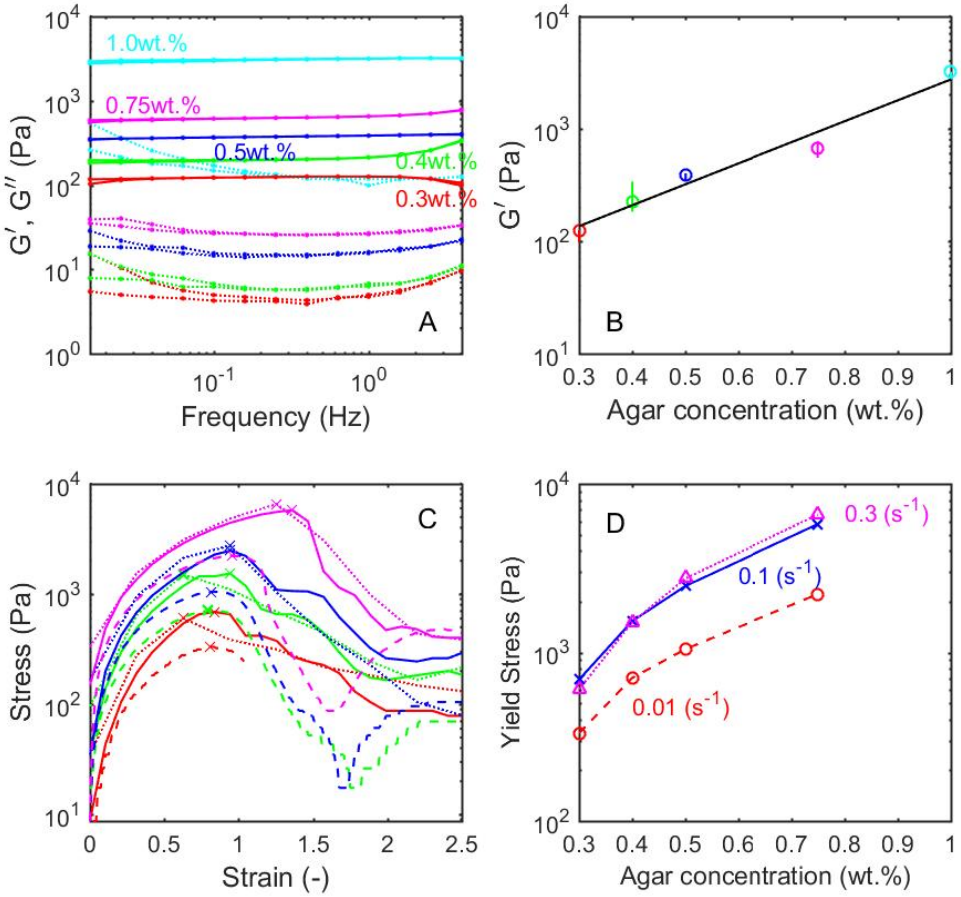

Figure DR3.

Rheological properties of agar gel. (A) Storage G'(solid curve) and loss G'' (dotted curve) moduli, measured by oscillatory deformation, with a strain amplitude of 10^{-3}, using Anton paar MCR102 rheometer. The color of the curves indicates different agar concentrations. In all measurements, $G' \gg G''$, i.e., the agar is elastic. We thus use G' as the shear modulus G. (B) The dependence of G' on the agar concentration at a frequency of 1.6 Hz. The error bars show the variability for the range of frequencies shown in (A). (C) Stress evolution under one-way rotation of a vain spindle with a diameter of 5.9 mm, and a length of 12 mm, measured by Brookfield DV2HB viscometer. The sharp stress decrease at a strain of 0.8-1.3 indicates the agar gel yield threshold (Sumita and Ota, 2011). The dashed, solid and dotted curves are for the strain rates of 0.01, 0.1 and 0.3 s^{-1}, respectively, where we use the displacement angle and angular velocity divided by π as the strain and strain rate, respectively. The color of the curves is the same as that in (A). (D) The dependence of yield stress on agar concentrations. The color of the symbols and curves indicate the different strain rates. (C, D) indicate that the yield threshold of this agar gel is around the strain of 1.

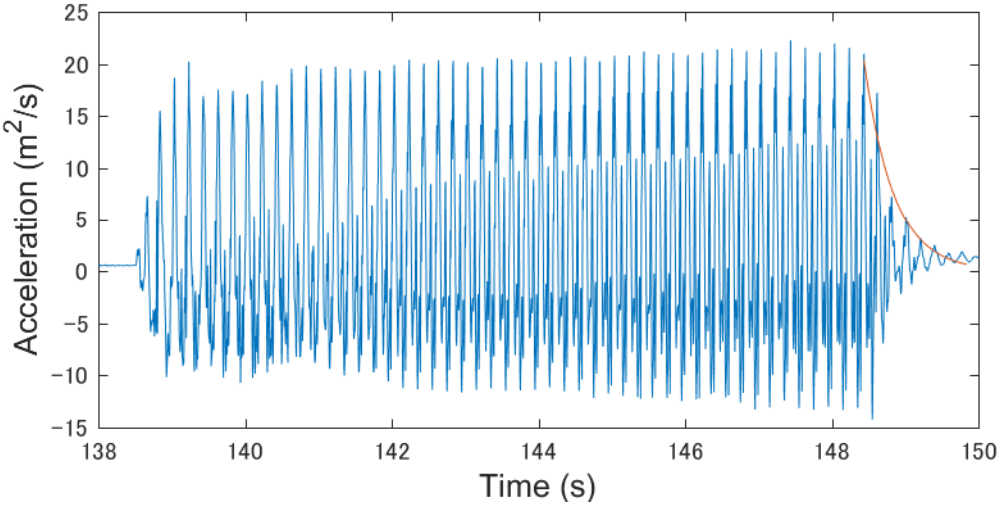

Figure DR4.

Acceleration, measured by a sensor located at the top of the gel edifice, which has a height of 145 mm, a top width of 45 mm and a shear modulus of 1300 Pa, oscillating with a frequency of $f = 5$ Hz and a displacement amplitude of 3 mm. When the imposed oscillation stops, the acceleration amplitude reduces. The red curve indicates the fitting by the exponential decay, $\xi(t) = \xi_0 \exp\left(-\frac{\pi f t}{Q}\right)$, where $\xi(t)$ is the time dependent amplitude of the acceleration with an initial value of ξ_0, with $Q^{-1} = 0.16$. (Aki and Richards, 2004). The time scale for damping is <1 s.

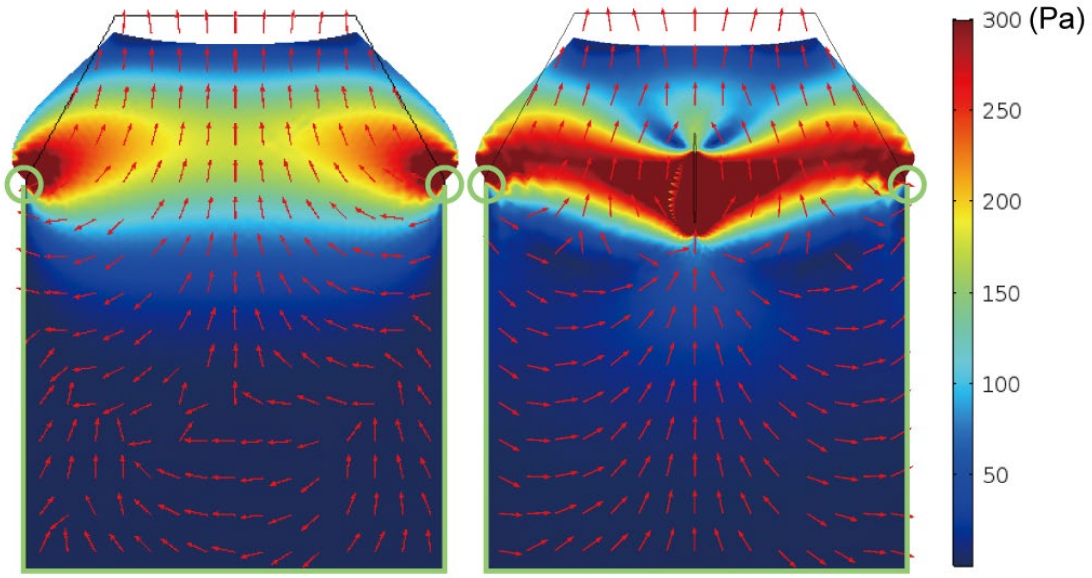

Figure DR5.

Calculated 2D stress field of the gel edifice used in our experiment (Fig.2) deformed by gravity without shaking. Left and right figures are without and with a crack, respectively. The crack is modeled as an ellipse with long and short radii of 15 mm and 0.5 mm, respectively. The lower half of the boundaries are fixed, as denoted by the green frames. The color indicates von Mises stress (Pa) and the arrows indicate the third principal stress direction. The black frame indicates the undeformed shape of the gel. Around the base of the edifice, the deviatoric stress is large so that a crack easily propagates horizontally at this depth. In the right figure, the stress at the upper crack tip becomes 1700 Pa. The solution is obtained by using a stationary solver in COMSOL.

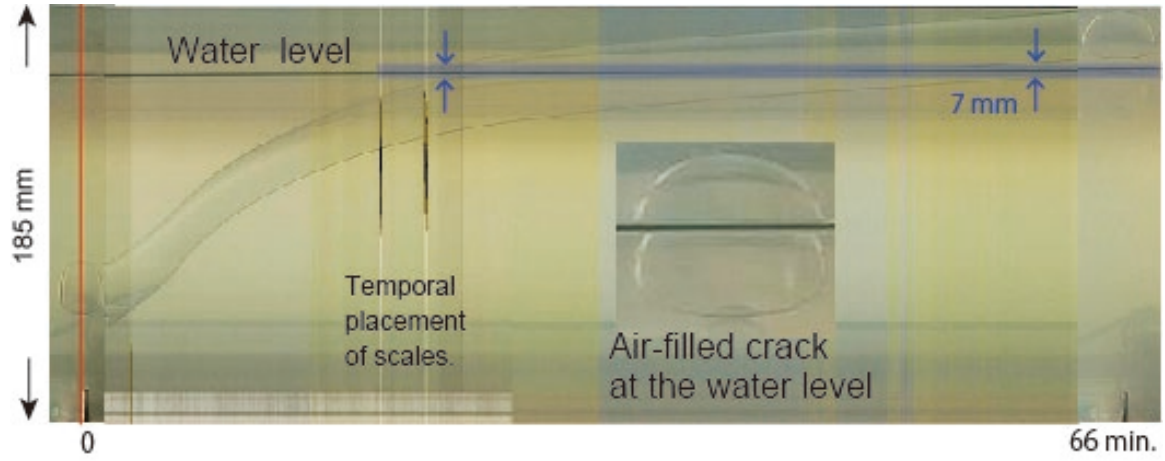

Figure DR6.

The method used in Fig.1B to remove the optical effect of the water interface. After removing the lid, a small amount of water, squeezed out of the gel, pools around the base of the gel edifice. Because of the discontinuity in the refraction index, the outline of the bubble around the water level duplicates, as shown by the inset picture in Fig. DR6. In order to remove this duplication, we extracted the time evolution of the height of the air-filled crack from the images. On the left- and right-hand sides, we show a picture of the ascending air-filled crack. In the middle, we see the time evolution of the upper and bottom edges of the air bubble in the crack, in the position of each frame occupied by the red line. From this picture, we conclude that a region of 7 mm around the water level duplicates, as shown by the blue arrows and the blue bar, so we remove this region. Vertical lines indicate times and heights where scales are placed temporarily in front of the cameras.

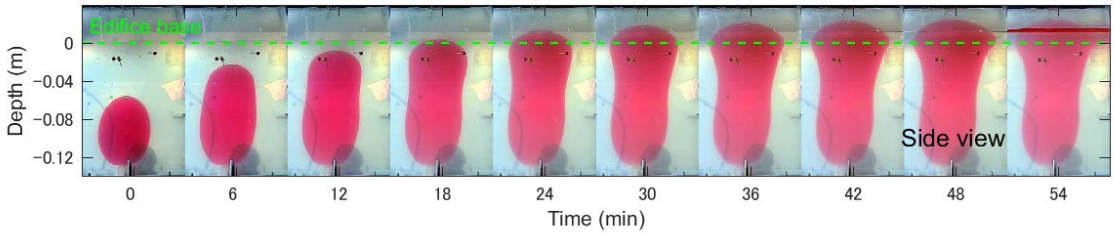

Figure DR7.

Same as for Fig.1B but for Fig.1D. The width of the water-filled crack is wider than the air-filled crack (Fig.1C). This is because, if there are no deviatoric stress, the maximum width of a crack is determined by the balance between the elastic and buoyancy forces,$[GV_{\mathrm{b}}/\{(1-\upsilon)\Delta\rho g\}]^{1/4}$, where $V_{\mathrm{b}}$is the volume of the buoyant fluid, and υ is the Poisson ratio (Taisne et al., 2011). This equation indicates that a crack with a smaller density difference and larger volume has larger width. This tendency must be the same even under a deviatoric stress. The water-filled crack shown in Fig.1D can be three times wider than that shown in Fig.1C. This estimate is consistent with our observation (Fig.1C, 1D). In addition, at the depth of the edifice base, the edifice modifying stress field makes the crack spread horizontally (Fig.DR5). As a result, the water-filled crack reaches the sidewall prior to erupting from the top of the edifice. In this figure, the discontinuity in the refraction around the water level is removed by the same method used in Fig. DR6.

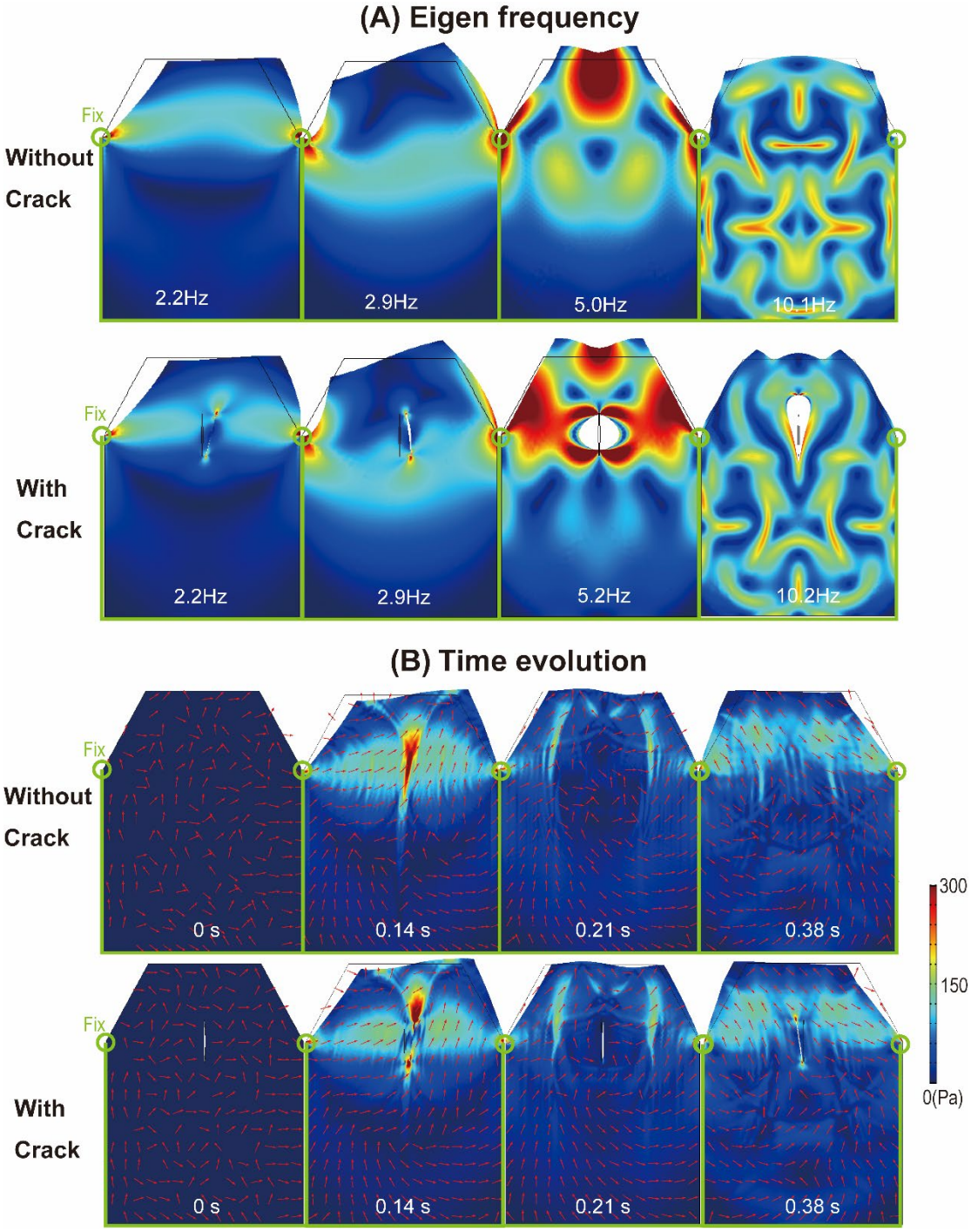

Figure DR8.

Results of a 2D numerical simulation with the same dimensions and gel properties of the experiment shown in Fig.2. (A) The deformation (shape) and stress patterns (color) of several modes at different eigen frequencies. The color difference shows the relative magnitude of the von Mises stress. The panels in the upper and lower rows indicate the results without and with a crack, respectively. The crack is modeled as an ellipse with long and short radii of 15 mm and 0.5 mm, respectively. The solution is obtained by using an eigen frequency study in COMSOL, which calculates the harmonic solution of the wave equation with a linear assumption. The black frame

and ellipse indicates the undeformed shape of the gel and the crack. The lower half of the boundaries are fixed. The left side three panels list results in several solutions resembling our experiments (2.2~5.2 Hz). The calculated eigen frequencies are the same orders of magnitude as the resonance frequencies obtained through other methods (Table DR1). The higher order solutions (~10 Hz) do not clearly appear in experiments (Movie DR1). (B) The time evolution of the deformation and stress field by imposing an initial velocity of 0.094 m s^{-1}. This initial velocity is calculated as $2\pi Af$, where $A = 3$ mm, and $f = 5$ Hz, the same conditions as used in Fig.2. The red arrows indicate the direction of the first principal stress. The solution is obtained by using a time-dependent study in COMSOL, which calculates the equation of motion. The time showing each panel corresponds to the local minima and maxima of the time dependent stresses at the crack tip shown in Fig.DR9. Because of technical reasons, gravitational forces are not considered in this figure.

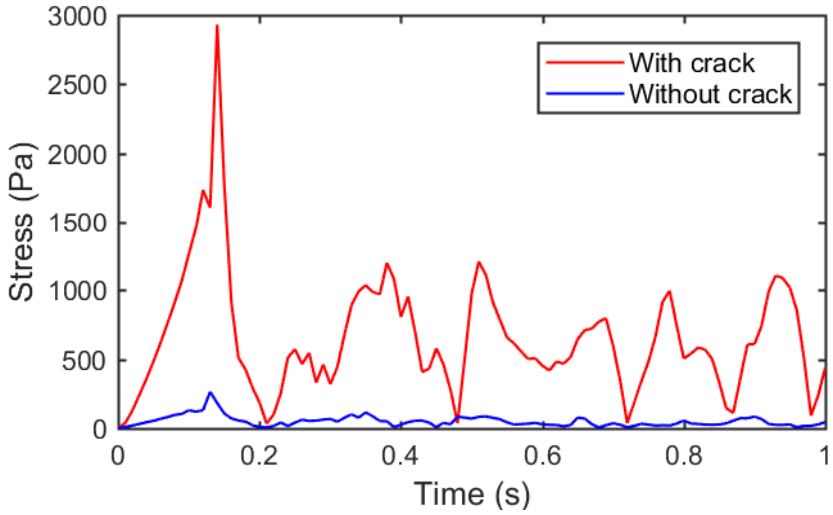

Figure DR9.

The time evolution of the von Mises stress during the oscillation of the gel edifice shown in Fig.DR8B. For the case with a crack, we plot the stress at the upper crack tip. For the case without a crack, we plot the stress at the center of the edifice base. When a crack exists, the maximum stress becomes close to 3000 Pa which is larger than the stress induced by the gravitational force, 1700 Pa (Fig.DR5), and comparable to the yield stress of our most frequently used gel with the agar concentration of 0.5 wt.% (Fig.DR3).

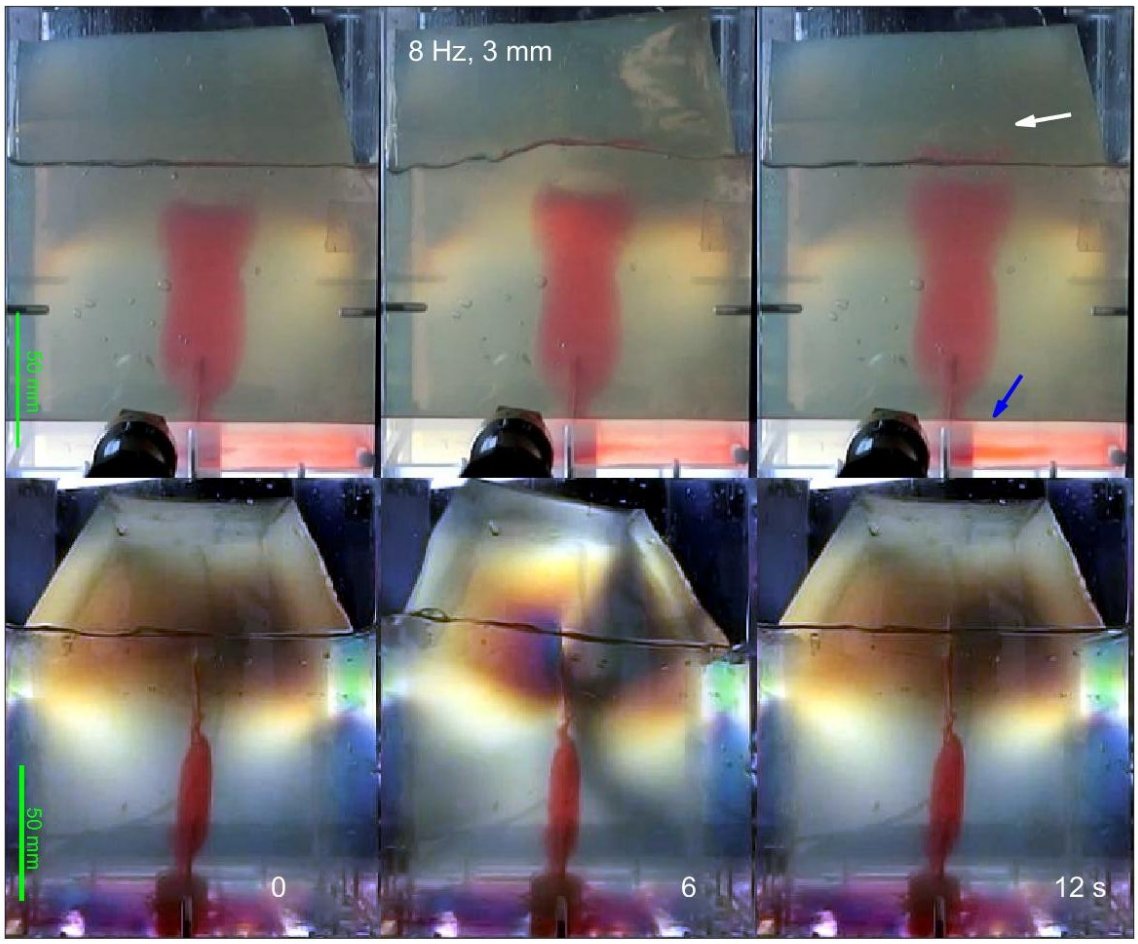

Figure DR10.

Simultaneous ascent and descent of the red-dyed bubbly fluid upon shaking. The injection had a volume of 6 mL, a viscosity of 0.9 Pa s, a liquid density of 1000 kg m^{-3}, and a bubble fraction of 5 vol.%, in a gel with a shear modulus of 320 Pa, a density of 1140 kg m^{-3}, and the resonance frequency of 3.5 Hz. We impose shaking at a frequency of 8 Hz and an amplitude of 3 mm for 10 seconds. Bubbles accumulate at the top of the crack (white arrow), while the denser liquid descends (blue arrow). The stress field is visualized by photoelasticity. (Top row) Side view. (Bottom row) Front view. Seconds indicate the elapsed time after the initiation of the shaking.

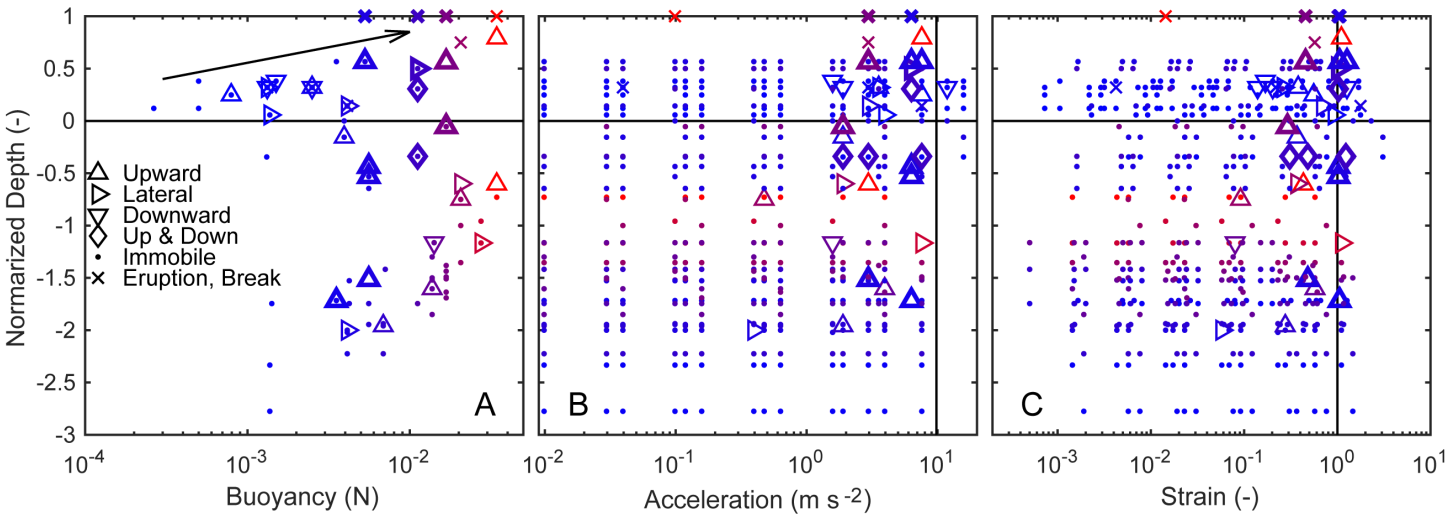

Figure DR11.

Responses of cracks filled with buoyant fluids to shaking. (A) Direction of crack propagation upon shaking, mapped as a function of the buoyancy force and depth of the crack tip at the onset of shaking, normalized by the gel edifice height. The symbols are the same as in Fig.4A, excepting the cross showing that the buoyant fluid reaches the summit or edges of the gel edifice. The symbol color indicates the buoyancy force. The buoyancy force is calculated by $\Delta\rho g V_{\mathrm{b}}$. The maximum reachable height increases with the buoyancy force, as denoted by the black arrow, indicating that a fluid with a larger buoyancy force can ascend to a shallower depth. When the buoyancy force is not sufficiently large, or the buoyant fluid is located deeper than the base of the gel edifice, the fluid-filled cracks sometimes migrate laterally or downward upon shaking, as denoted by the inverted and rightward triangles. (B) Dependence on the acceleration, $A\omega^2$. As the acceleration increases, the buoyant fluid tends to respond more frequently. (C) Dependence on the average strain generated by the gel edifice resonance at the base of the edifice. The average strain is calculated by $MA\omega^2/W^2/G$, where M is the mass of the gel edifice. When the strain reaches unity, the fluid-filled cracks propagate, which is consistent with the measured yield threshold shown in Fig.DR3. In some experiments, the fluid-filled cracks can propagate even when the strain is less than unity, suggesting the occurrence of strain localization by the existence of a crack, and amplification by resonance.

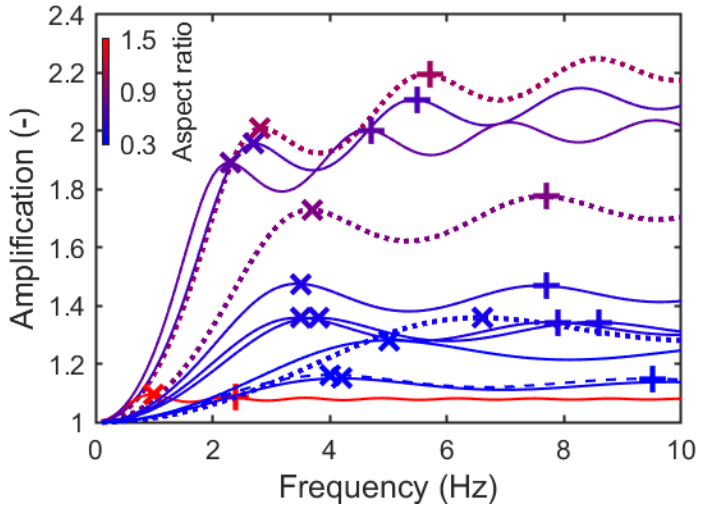

Figure DR12.

Calculated amplification by Eq.(DR3) for our gel edifices between the input of the shear horizontal motion at the bottom with respect to the surface. The color of the curves indicates different edifice aspect ratios, as denoted in the color bar; the reddish and bluish colors indicate the relatively tall and flat edifice shapes, respectively. Local maxima indicate resonance frequencies; the cross is the fundamental mode and the plus is the second mode. The dashed, solid, and dotted curves indicate the different shear moduli of the agar gel, approximately 210, 320, and >9000 Pa, respectively.

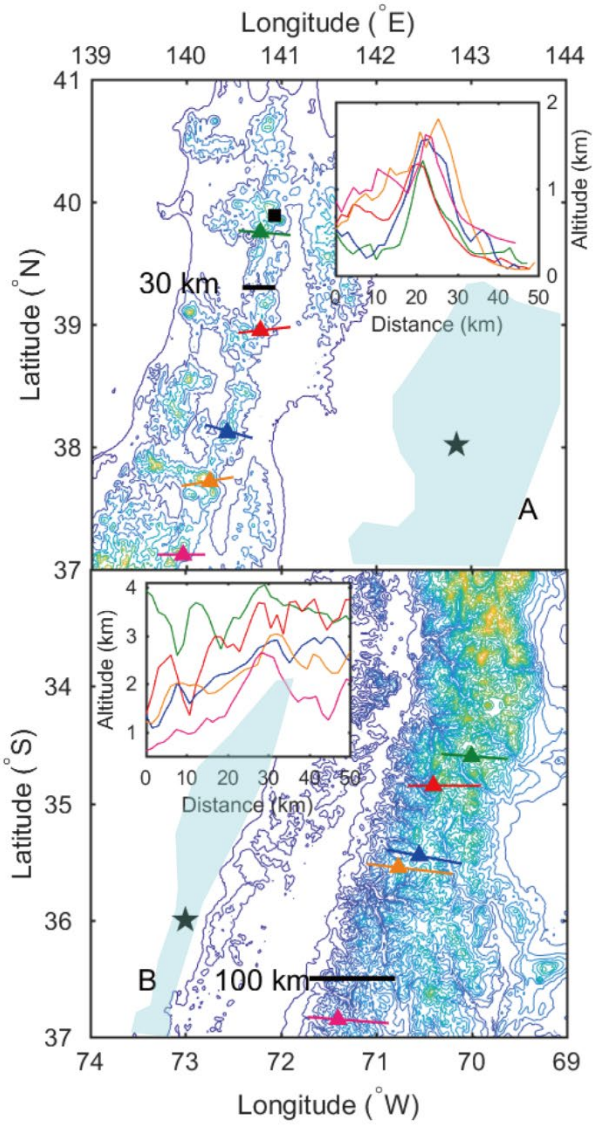

Figure DR13.

The contour maps of the volcanic ranges, where subsidence was observed after the Tohoku (A) and the Maule (B) earthquakes (Amante and Eakins, 2009). The contour interval is 300 m. Triangles indicate the locations of subsidence, and the stars and blue regions indicate the epicenters and rupture areas of large earthquakes, respectively. Insets indicate the elevation profiles where subsidence is observed. The locations of the profiles are shown in the contour maps, using the same colored lines as in the insets. The black square indicates the seismic station from which data is shown in Fig.DR15.

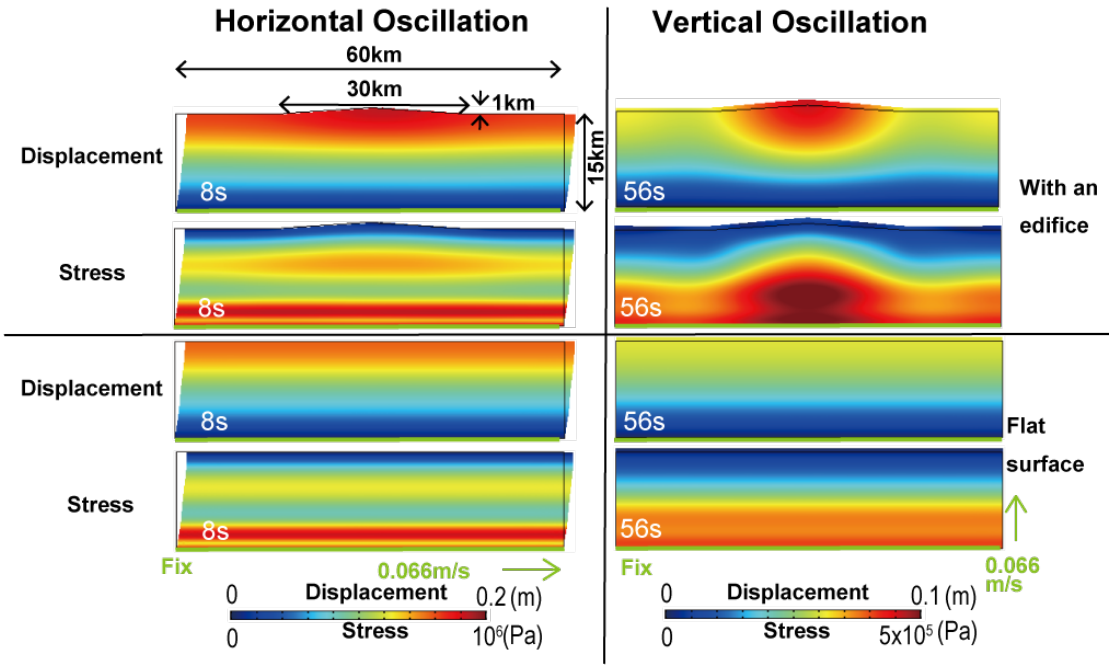

Figure DR14.

Results of 2D numerical simulations of horizontal/vertical oscillation of a 15 km thick layer with a shear modulus of 3×10^{10} Pa, a Poisson ratio of 0.28 and a shear wave velocity of 3 km s^{-1}. The panels in the upper two rows include a surface topography simulating a volcanic range, and the lower two rows have a flat surface. The volcanic range has a width of 30 km and height of 1 km, similar dimensions to the volcanic range in Tohoku, where subsidence was observed (Fig.DR13). The layer thickness of 15 km is similar to that of the upper crust (e.g., Xia et al., 2007). The resonance frequency of both the volcanic range and the horizontal layer are on the order of 0.1 Hz. As an initial condition, we impose a velocity of 0.066 m s^{-1}, calculated from a displacement amplitude of 0.1 m and a frequency of 0.1 Hz, in both the horizontal and vertical directions, and observe its time evolution. The bottom boundary is fixed and others are free. The right and left boundaries obey periodic boundary conditions. The layer oscillates in the horizontal and vertical directions according to the initial velocity. In the simulations with a volcanic range, the deformation and stress patterns change. The white numbers indicate the elapsed time after the calculation begins. The solution is obtained by using a time dependent study in COMSOL.

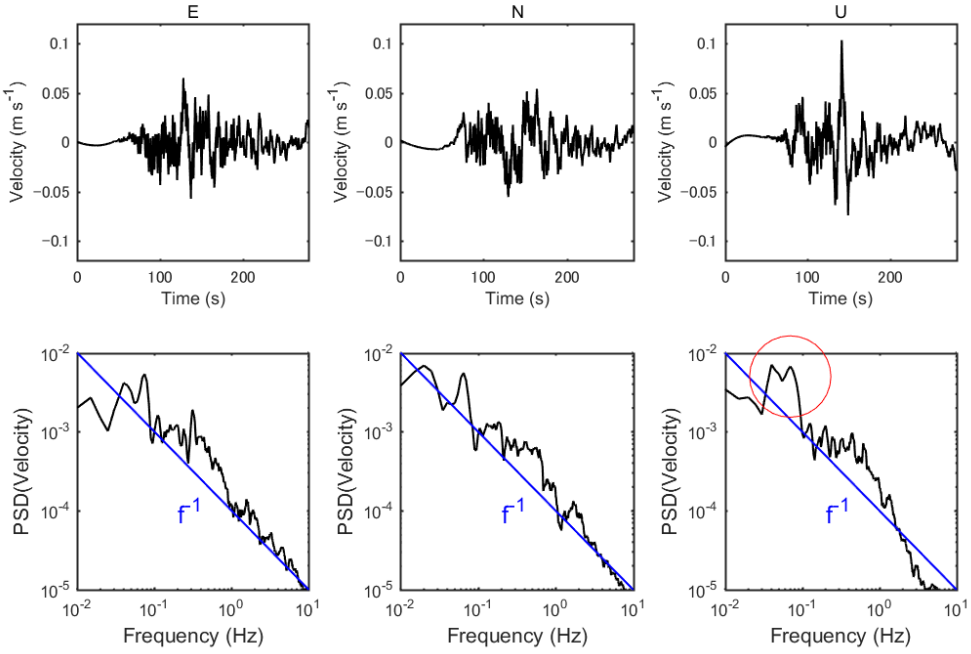

Figure DR15.

Seismograms of the Tohoku earthquake in the East-West, North-South, Up-Down directions observed at Iwate Mountain, marked as a black square in Fig.DR13, through V-net (NIED), and their power spectra between 60-260s. The frequency response <1Hz is corrected according to the instrument response. The spectra are smoothed in the range of $\pm 0.05f$ around the corresponding frequency f. Essentially, the spectra follow the widely known trend f^{-1}. However, the vertical oscillation shows a peak around 0.07 Hz, as denoted by the red circle, which is consistent with the estimated resonance frequency of the volcanic range. The oscillation in the East-West direction may also suggest a peak around the resonance frequency.

Table DR1 Experimental conditions [a].

H	H_b	w_t	G'	Agar density	v_s	$0.7v_s/W$	Mode1	Mode2	Numerical	Fluid density	Fluid volume	Type*	
mm	mm	mm	Pa	kg m^{-3}	m s^{-1}	Hz	Hz	Hz	Hz	kg m^{-3}	mL		
125	20	45	1300	1140	1.06	5.3	3.7	7.7	2.2,4.4,7.8	1113	0, 1, 3, 5	1	
150	20	27	950	1134	0.91	4.6	2.8	5.7	1.6, 3.2, 5.6	1083	0, 1, 3, 5	2	
90	60	30	320	1134	0.53	2.6	2.7	5.5	1.7, 2.6, 5.1	1000	0, 1, 3	3	
0	215	120	350	1134	0.56	2.8	-	-	-	1000	0, 1, 3, 5, 10, 20	4	**rectangular
105	50	34	320	1140	0.53	2.6	2.3	4.7	1.4, 2.4, 4.8	1000	1,3	5	
48	150	110	340	1140	0.54	2.7	4.2	9.7	2.3, 3.1, 4.7	1000	0, 1, 3, 5, 10, 15, 20, 25	5	Fig.3
40	150	108	210	1140	0.43	2.1	4.0	9.5	2.1, 2.6, 4.0	1000	0, 1, 3, 5, 10, 15	5	
55	130	80	970	1144	0.92	4.6	6.6	>10	3.8, 5.1, 8.6	1000	0, 1, 3, 5, 10	6	
62	100	67	320	1140	0.53	2.7	3.5	7.7	2.1, 2.8, 5.1	950	3, 6	5	Fig.DR10
60	130	80	320	1144	0.53	2.6	3.5	7.9	2.1, 2.8 4.9	960	2, 3	4	
55	130	80	320	1140	0.53	2.6	3.8	8.6	2.2,2.9,5.0	1	0.5, 1, 1.5	5	Fig.2
55	130	80	320	1140	0.53	2.7	3.8	8.6	2.2,2.9,5.0	1	0.5, 1, 1.5	-	Fig.1
40	140	90	310	1141	0.52	2.6	5.0	>10	2.6, 3.2, 5.2	1000	15	-	Fig.1

Type	Amplitude mm	Frequency Hz
1	1	0.5, 1, 2, 4, 10, 20
	3	0.5, 1, 2, 4, 5
2	1	0.5, 1, 2, 4, 10, 20
	3	0.5, 1, 2, 4, 5, 8
	10	0.5, 1, 2, 3
3	1	0.5, 1, 2, 4, 10, 20
	3	0.5, 1, 2, 4, 5, 8
	10	0.5, 1, 2
4	1	0.5, 1, 2, 4, 10
	3	0.5, 1, 2, 4, 5, 8
	10	0.5, 1, 2, 3, 4
5	1	0.5, 1, 2, 4, 10
	3	0.5, 1, 2, 4, 5, 8
	10	0.5, 1, 2
6	1	0.5, 1, 2, 4, 10
	3	0.5, 1, 2, 4, 5
	10	0.5, 1, 2

[a]: Dimensions of the gel edifice are shown in Fig.DR1. The storage modulus G', as the shear modulus, is calculated by the fitting line in Fig.DR3B. Mode 1 and 2 are the fundamental and second mode of the resonance frequencies of the gel edifice, calculated by Eq.(DR3), respectively. The label “Numerical” indicates the eigen frequencies, calculated by the method in Fig.DR8. We did not calculate the resonance frequencies for the gel in a rectangular shape. *: Type indicates the combination of the oscillation amplitude and frequencies, listed separately. We here list the typical oscillation sequences. When the gel broke, the oscillation sequence was modified.

Table DR2 Parameters and non-dimensional numbers [b].

Parameters	Symbols	Unit	Experiments	Natural volcanoes
Height	H	m	0.04-0.2	10^3-5x10^3
Width	W	m	0.14	10^4-3x10^5
H/W		-	0.15-1.5	0.03-0.1
Shear modulus	G	Pa	200-1300	~3x10^{10}
Host rock density	ρ	kg m^{-3}	~10^3	~3x10^3
S wave velocity	v_s	m s^{-1}	0.4-1	~3x10^3
v_s/W		Hz	3-8	0.1
Dike length	l	m	10^{-2}-2x10^{-1}	<10^3
Fluid density	ρ_i	kg m^{-3}	1-10^3	1-3x10^3
Buoyancy Pressure in a dike	$(\rho-\rho_i)gl$	Pa	300 (0.03m, $\Delta\rho$=10^3 kg m^{-3})	~5x10^5 (500 m, $\Delta\rho$=100 kg m^{-3})
Inertia induced stress acting on the base	σ_b $[(MA\omega^2)/W^2]$	Pa	100-300 (A=3mm,f=5Hz)	3x10^5-10^6 (A=0.5m, f=0.1Hz)
Strain	γ $[(MA\omega^2)/(GW^2)]$	-	~1	~10^{-5}
Fracture pressure	P_F	Pa	~10^3	~10^6-10^8
Attenuation	Q^{-1}		~10^{-1}	~10^{-3}

Non-dimensional numbers

σ_b/P_F	-	-	0.1-0.3	0.003-1
$(\rho-\rho_i)gL/P_F$	-	-	0.3	0.005-0.5
$\sigma_b/(\rho-\rho_i)gL$	-	-	0.3-1	0.6-2

[b]: Comparison between the experiments and natural volcanoes. Parameters used in experiments are listed in Table DR1. The dimensions for natural volcanoes are estimated from volcanic ranges in the southern Andes, Chile and Tohoku, Japan, in which subsidence is observed. The shear modulus G and host rock density are ordinary values (e.g., Turcotte and Schubert, 2014). The vertical length of the magma storage can be as long as several km, equivalent to the edifice height (Browne and Szramek, 2015). The density of the fluid in the crack must be between that of volcanic gases ρ_i=1 kg m^{-3} and basaltic magma ρ_i<3000 kg m^{-3}. Water density (ρ_i=1000 kg m^{-3}) is within this range. Regarding the mass of volcanic edifice M, we assume that the volcanic range is 2D, so that the inertia-induced stress, acting on the edifice base, is $\rho HA\,\omega^2/2$. Dividing the inertia-induced stress by the shear modulus produces a strain $\gamma=\rho HA\,\omega^2/(2G)$. We use the fracture stress of a gel with 0.5 wt.% agar as the set value for all the experiments (Fig.DR3). The fracture toughness of natural rocks in atmospheric conditions is K_c~10^6-10^8 Pa m$^{1/2}$ (e.g., Lister, 1990; Balme et al. 2004, Rivalta et al., 2015). If the dike width is several meters, the fracture pressure becomes ~10^6-10^8 Pa. Q^{-1} in the experiments are estimated by the ratio of G''/G' (Fig.DR3), and the measured damping (Fig.DR4). Q^{-1} for natural rocks is calculated from Q for S waves (Liu et al., 2014). In both experiments and natural volcanoes, the inertia-induced stress σ_b and the buoyant stress $(\rho-\rho_i)gl$ are approximately the same as the fracture pressure, P_F.

Movie DR1

A movie of Fig.2, 0-3s. An accelerated ascent of the air-filled crack caused by external oscillation with a frequency of 5 Hz and amplitude of 3 mm, in a gel edifice with a density of 1140 kg m^{-3} and shear modulus of 320 Pa. The crack includes dry air with a volume of 1.5 mL, a density of 1 kg m^{-3}, and a viscosity of 2×10^{-5} Pa s. The external oscillation is in the right-left direction in the front view. The side and top cameras are located on the ground, so record the displacement of the tank relative to the ground. The front camera is mounted on the shaking table so records the deformation of the gel edifice relative to the tank, and sometimes the backlash. The side camera is located on the left side of the front view. This video is approximately 8 times slower than real time. The front and side cameras are 240 fps and synchronized. The top camera is 60 fps and does not synchronize with the other two cameras.

Movie DR2

A movie of Fig.3, 0-10s. An accelerated ascent of red-dyed water by an external oscillation with a frequency of 5 Hz and amplitude of 3 mm, in a gel edifice with a density of 1140 kg m^{-3} and shear modulus of 340 Pa. The injected water has a volume of 25 mL, a density of 1000 kg m^{-3}, and a viscosity of 10^{-3} Pa s. This video is approximately 8 times slower than real time. The camera settings are the same as for Movie DR1.

Movie DR3

A movie corresponding to Fig.3, 14-17s. When the shaking at 8 Hz begins, the buoyant fluid reaches the left side of the tank wall in the side view, and then reaches summit. This video is approximately 8 times slower than real time. The other settings are the same as Movie DR2.

Movie DR4

A movie of Fig.DR10. Simultaneous ascending and descending of the red-dyed bubbly fluid with a volume of 6 mL, viscosity of 0.9 Pa s, liquid density of 1000 kg m^{-3}, and bubble fraction of 5 vol.%, in a gel with shear modulus of 320 Pa, and density of 1140 kg m^{-3}. The imposed oscillation is at a frequency of 8 Hz and an amplitude of 3 mm for 10 seconds. Bubbles accumulate at the top of the crack, while the liquid descends, as shown by the blue arrow. This video is approximately 8 times slower than real time.

Movie DR5

Movies of Fig.DR14 with a surface topography for 60 s.

REFERENCES CITED

Aki, K., and Richards, 2004, Quantitative Seismology, 2nd Edition, Kokin-shoin, Tokyo, Japan, p. 909.

Amante, C., and Eakins, B.W., 2009, ETOPO1 1 Arc-Minute Global Relief Model: Procedures, Data Sources and Analysis. NOAA Technical Memorandum NESDIS NGDC-24. National Geophysical Data Center, NOAA. doi:10.7289/V5C8276M.

Balme, M.R., Rocchi, V., Jones, C., Sammonds, P.G., Meredith, P.G., Boon, S., 2004, Fracture toughness measurements on igneous rocks using a high-pressure, high-temperature rock fracture mechanics cell: Journal of Volcanology and Geothermal Research, v.132, p.159–172.

Browne, B., and Szramek, L., 2015, Rates of magma ascent and storage: In The encyclopedia of volcanoes: Edited by Sigurdsson, Academic Press, London, U.K., p.203-214.

Brune, J. N., 1996, Particle motions in a physical model of shallow angle thrust faulting: Proceedings of the Indian Academy Of Science (Earth Planet. Sci.), v. 105, p.L197–L206.

Gabuchian, V., Rosakis, A. J., Bhat, H. S., Madariaga, R., and Kanamori, H., 2017, Experimental evidence that thrust earthquake ruptures might open faults: Nature, v. 545(7654), p.336-339.

Geli, Li., Bard, P.-Y., and Jullien, B., 1988, The effect of topography on earthquake ground motion: A review and new results: Bulletin of the Seismological Society of America, v. 78, p.42-63.

Kavanagh, J. L., and Menand, T., and Daniels, K., 2013, Gelatine as a crustal analogue: determining elastic properties for modelling magmatic intrusions: Tectonophysics, v. 582, p.101–111.

Karlstrom, L., Dufek, J., and Manga. M., 2009, Organization of volcanic plumbing through magmatic lensing by magma chambers and volcanic loads: Journal of Geophysical Research, v.114, B10204, doi:10.1029/2009JB006339.

Koketsu, K., Yokota, Y., Nishimura, N., Yagi, Y., Miyazaki, S., Satake, K., Fujii, Y., Miyake, H., Sakai, S., Yamanaka, Y., and Okada, T., 2011, A unified source model for the 2011 Tohoku earthquake: Earth and Planetary Science Letters, v.310, p. 480-487.

Lister, J. R., 1990, Buoyancy-driven fluid fracture: similarity solutions for the horizontal and vertical propagation of fluid-filled cracks: Journal of Fluid Mechanics v.217, p.213–239.

Lister, J. R., and R. C. Kerr, 1991, Fluid-mechanical models of crack propagation and their application to magma transport in dykes: Journal of Geophysical Research, v.96(B6), p.10049‑10077, doi: 10.1029/91JB00600.

Liu, X., Zhao, D., and Li, S., 2014, Seismic attenuation tomography of the Northeast Japan arc: Insight into the 2011 Tohoku earthquake (Mw 9.0) and subduction dynamics: Journal of Geophysical Research- Solid Earth, v. 119, p. 1094–1118, doi:10.1002/2013JB010591.

Maccaferri, F., Bonafede, M., and Rivalta, E., 2011, A quantitative study of the mechanisms governing dike propagation, dike arrest and sill formation: Journal of Volcanology and Geothermal Research, v. 208, p.39–50.

Pinel, V., and Jaupart, C., 2000, The effect of edifice load on magma ascent beneath a volcano: Philosophical Transactions of Royal Society London, Series A, v. 358, p.1515–1532.

Rivalta, E., Taisne, B., Bunger, A. P., and Katz, R. F., 2015, A review of mechanical models of dike propagation: Schools of thought, results and future directions: Tectonophysics, v.638, p.1-42.

Rubin, A.,1995, Propagation of Magma-Filled Cracks: Annual Review of Earth and Planetary Sciences, v. 23, p. 287-336.

Sumita, I., and Ota, Y., 2011, Experiments on buoyancy-driven crack around the brittle–ductile transition: Earth and Planetary Science Letters, v.304, p.337-346.

Takada, A., 1990, Experimental study on propagation of liquid-filled crack in gelatin: shape and velocity in hydrostatic stress condition: Journal of Geophysical Research, v. 95, p.8471–8481.

Turcotte, D. L., and Schubert, G., 2014, Geodynamics: Cambridge University Press, Cambridge, U.K., p. 623.

Willey, T., 2017, Stress Calculations and Dynamic Photoelasticity: Bachelor thesis, University of Montana and University Potsdam, Montana, USA and Potsdam, Germany, p.27.

Xia, S., Zhao, D., Qiu, X., Nakajima, J., Matsuzawa, T., and Hasegawa, A., 2007, Mapping the crustal structure under active volcanoes in central Tohoku, Japan using P and PmP data: Geophysical Research Letters, v. 34, L10309, doi:10.1029/2007GL030026.